ACS NANO

www.acsnano.org

ARTICLE

Colossal Core/Shell CdSe/CdS Quantum Dot Emitters

Hao A. Nguyen, Benjamin F. Hammel, David Sharp, Jessica Kline, Griffin Schwartz, Samantha Harvey, Emily Nishiwaki, Soren F. Sandeno, David S. Ginger, Arka Majumdar, Sadegh Yazdi, Gordana Dukovic, and Brandi M. Cossairt*

Cite This: *ACS Nano* 2024, 18, 20726–20739

Read Online

ACCESS | Metrics & More | Article Recommendations | Supporting Information

ABSTRACT: **Single-photon sources are essential for advancing quantum technologies with scalable integration being a crucial requirement. To date, deterministic positioning of single-photon sources in large-scale photonic structures remains a challenge. In this context, colloidal quantum dots (QDs), particularly core/shell configurations, are attractive due to their solution processability. However, traditional QDs are typically small, about 3 to 6 nm, which restricts their deterministic placement and utility in large-scale photonic devices, particularly within optical cavities. The largest existing core/shell QDs are a family of giant CdSe/CdS QDs, with total diameters ranging from about 20 to 50 nm. Pushing beyond this size limit, we introduce a synthesis strategy for colossal CdSe/CdS QDs, with sizes ranging from 30 to 100 nm, using a stepwise high-temperature continuous injection method. Electron microscopy reveals a consistent hexagonal diamond morphology composed of 12 semipolar $\{10\bar{1}1\}$ facets and one polar (0001) facet. We also identify conditions where shell growth is disrupted, leading to defects, islands, and mechanical instability, which suggest synthetic requirements for growing crystalline particles beyond 100 nm. The stepwise growth of thick CdS shells on CdSe cores enables the synthesis of emissive QDs with long photoluminescence lifetimes of a few microseconds and suppressed blinking at room temperature. Notably, QDs with 80 and 100 CdS monolayers exhibit high single-photon emission purity with second-order photon correlation $g^{(2)}(0)$ values below 0.2.**

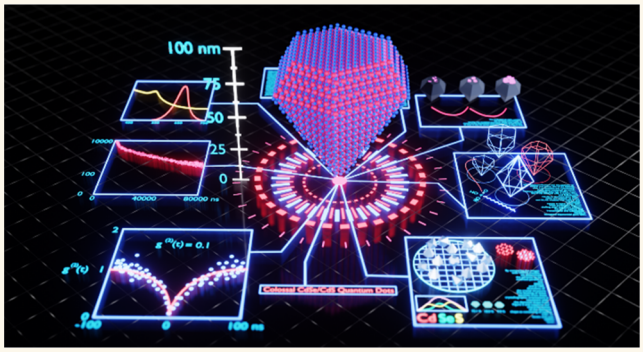

KEYWORDS: *quantum dots, nanocrystals, single-photon sources, semiconductor core/shell materials, light emission, electron microscopy*

INTRODUCTION

Single-photon sources are key components in advancing next-generation quantum technologies, wherein photons are employed as information carriers.[1−3] Extensive interdisciplinary research conducted over the past several decades has identified a variety of materials that can be used as single-photon sources, including trapped ions,[4,5] diamond color centers,[6,7] two-dimensional materials,[8,9] small molecules,[10,11] and semiconducting quantum dots.[3,12,13] Each class of materials presents advantages and limitations in single-photon emission performance and device integration. For these materials to be practically applied in quantum devices, a crucial requirement is scalability.[14−16] This involves the deterministic positioning of identical single-photon sources into large arrays, which can then be integrated with functional nanophotonic structures. In this context, colloidal quantum dots (QDs), especially core/shell and perovskite QDs, are the most promising candidates due to their solution processability, which facilitates large-scale synthesis and integration into nanoscale devices.[14,15,17−19]

While a colloidal QD itself can generate single photons, its potential for practical applications as a single-photon source, even for very high-quality QDs, is intrinsically limited due to ensemble inhomogeneity and batch-to-batch variation,[20] nondirectional emission,[21] photon losses in the substrate,[22] distinguishable photons emitted from the same QD,[23] and low single-photon generation rates, except for lead halide perovskite QDs.[24−26] To improve upon the current state of the art, an integrated system is required.[1,14,23,27] More specifically, a

Received: May 25, 2024
Revised: July 11, 2024
Accepted: July 17, 2024
Published: July 26, 2024

https://doi.org/10.1021/acsnano.4c06961
ACS Nano 2024, 18, 20726−20739

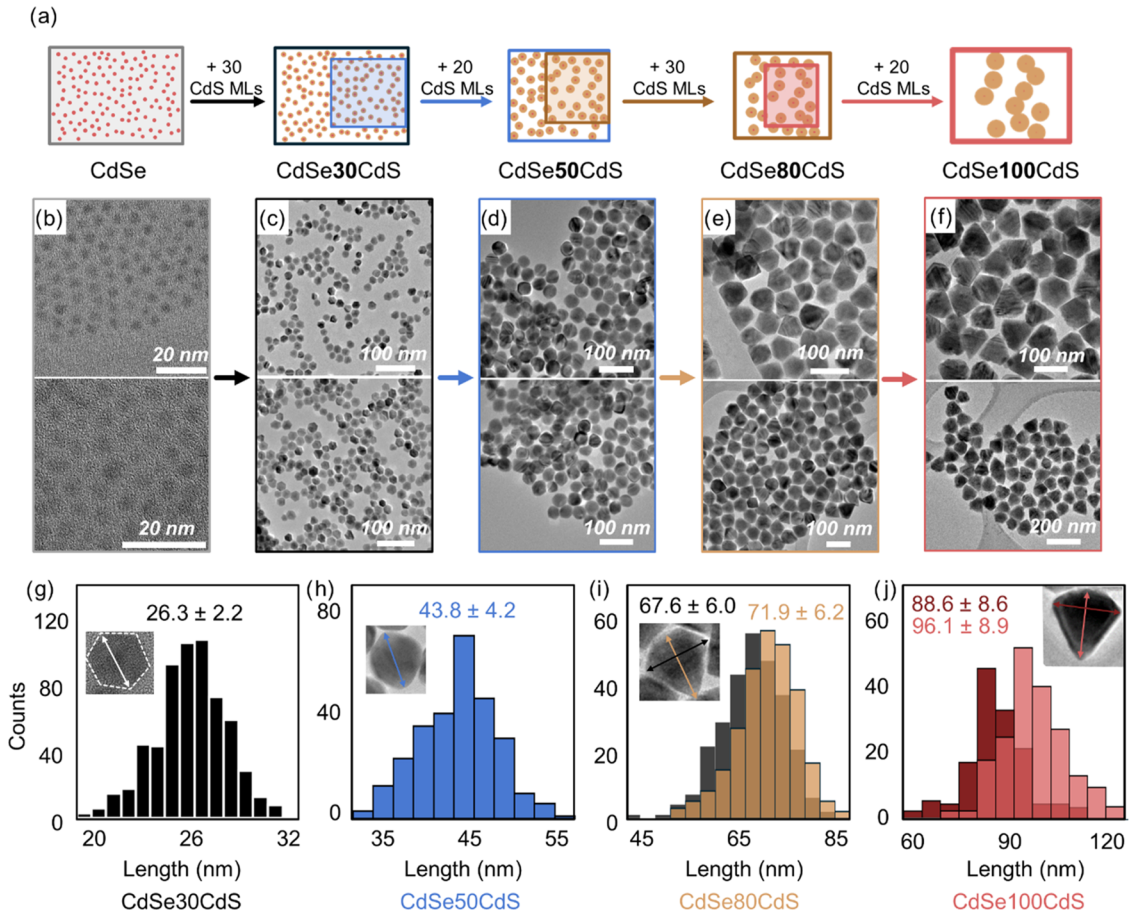

Figure 1. (a) Synthesis scheme for the stepwise CdS shelling of the CdSe cores. TEM images of CdSe cores (b) and resultant core/shell CdSe/CdS QDs with 30, 50, 80, and 100 CdS MLs (c–f) and their size distributions (g–j). Insets show a zoomed-in particle, where arrows indicate how measurements were made. In (i, j), the overlap of the two histograms is shown in the in-between color to represent the distribution of both sets of data.

QD single-photon emitter needs to be deterministically placed in the region of maximum electromagnetic field of an optical cavity for enhanced emission through the Purcell effect.[14,28] Current demonstrations of single-photon emission and cavity-coupling from QDs are often limited to random placement of single QDs on solid substrates[29,30] or manipulation of particle position via top-down fabrication tools,[31−34] thus providing no path for scalability. Meanwhile, large-scale placement of single nanoparticles requires substrates with nano- or microscale traps created through electron beam lithography, where the size compatibility between the traps and the particles is crucial.[14,15,30,35] Existing single-particle patterning techniques are typically less efficient with smaller particles. Therefore, increasing the size of the particles offers a promising solution to enhance the efficiency of this process.

QDs are small, with diameters typically ranging from ∼3 to 6 nm. Inorganic shells, typically Cd- and Zn-based, are grown on the cores to improve their chemical stability and photoluminescence (PL).[36] These core/shell QDs, composed of materials with different band gaps and band alignments, show a variety of optical properties due to their overall composition and shell thickness. Furthermore, external silica shells can be grown on core/shell QDs to increase the particle size to near 100 nm.[17,37] Although silica shells provide a path for deterministic positioning of emissive QDs, the single-particle PL of silica-shelled QDs suffers a high degree of blinking due to additional charged states induced by the CdS-SiO_2 interface.[17,38]

The largest emissive QDs without silica shells reported in the literature to date are the traditional quasi-type II giant core/shell CdSe/CdS QDs, with 15−20 CdS monolayers (MLs) and total diameters ranging from 20 to 50 nm.[39−42] The giant CdS shells not only increase the size of the emissive QDs but also reduce blinking through Auger recombination suppression and isolate the exciton from surface interactions.[39,43,44] In these quasi-type II core/shell systems, the electron wave function is delocalized into the CdS shell, while the hole wave function is effectively confined within the CdSe core. This geometric separation of charge carriers results in multiexciton formation that is advantageous for lasing and can affect the single-photon purity.[42,45−48]

The two main methods to grow large core/shell CdSe/CdS are successive ionic layer adsorption and reaction (SILAR) and high-temperature continuous injection (HTCI).[39,40,49] The differences between the two methods and the correlation between synthetic conditions and QD properties have been rigorously studied by Hollingsworth and co-workers.[39,40,50,51] By examining ∼20 nm, truncated octahedral QDs prepared by the two methods, they showed that while both methods result in nonblinking QDs with high stability, QDs prepared by the HTCI method have significantly higher PL quantum yield (QY) while QDs prepared by the SILAR method have better

https://doi.org/10.1021/acsnano.4c06961
ACS Nano 2024, 18, 20726−20739

optical stability at ambient conditions.[40] Further in-depth analysis revealed that high crystalline quality with high interfacial alloying and low defect concentrations in the CdS shells could be achieved with the HTCI method by postsynthetic annealing and the use of 1-octanethiol, which acts as both S precursor and growth-facilitating ligand.[40] Using the HTCI method but with S dissolved in ODE (S-ODE) as the sulfur precursor instead of 1-octanethiol, Dubertret and co-workers were also able to grow CdSe/CdS QDs with sizes up to 50 nm.[42] Meanwhile, Chen and co-workers have proposed three key design rules to form large, flat-faceted particles, including (1) slow epitaxial shell growth, (2) avoiding additional oleic acid, and postsynthesis annealing, which smooth out flat facets toward a spherical shape, and (3) intermediate purification steps to remove unreacted materials and byproducts for monodisperse products.[52] Leveraging these insights using the HTCI method enabled consistent syntheses of monodisperse bipyramidal wurtzite CdSe/CdS QDs with a longest dimension of 22 nm. In a different study, Bals and co-workers synthesized bullet-shaped CdSe/CdS QDs with a size of 30 nm using the SILAR method, and S-ODE.[41] These findings delineate the nuanced parameters for large QD synthesis and highlight an open question: what is the maximum QD size achievable without sacrificing the optical emission properties?

Motivated by the need for scalable and deterministic positioning of colloidal QD single-photon emitters in optical cavities, we introduce in this paper a series of "colossal" QDs, an extension of the class of giant QDs, with particle diameters exceeding 100 nm. We show that using a stepwise HTCI method with 1-octanethiol as our S precursor, we can systematically grow ultrathick CdS shells on wurtzite CdSe cores. The particle formation and morphology are studied by synthetic and electron microscopic analyses. The colossal QDs exhibit long PL lifetimes on the order of microseconds and suppressed blinking at room temperature. Surprisingly, high single-photon emission purity with low second-order photon correlation $g^{(2)}(0)$ values are observed even for QDs with 80 and 100 CdS ML shells.

RESULTS AND DISCUSSION

Synthesis of Colossal QDs. All samples in this study were synthesized by growing CdS shells on 3.5 nm wurtzite CdSe cores using a modified HTCI method.[49,52] Cadmium oleate and 1-octanethiol (both 0.2 M in ODE) were used as the shell growth precursors. The final size and the number of shell MLs of the resultant core/shell CdSe/CdS QD can be estimated by assuming spherical particles and a thickness for one CdS ML of 0.3375 nm. With this estimation, a direct HTCI synthesis of 50 nm core/shell CdSe/CdS QDs, starting from 50 nmol of CdSe cores, would require 350 mL of each precursor solution and a continuous injection period of 114 h at the standard rate of 3 mL/h—an approach that is unfeasible in most research laboratories (detailed calculation in the Supporting Information). Therefore, we sought to grow colossal QDs using a multistep growth strategy, wherein only a fraction of a previously synthesized batch is used for the next growth step.

The stepwise synthesis used to achieve 100 CdS MLs is described here as an example (Figure 1a) with detailed calculations of precursors and reaction volumes shown in the Supporting Information. Using the HTIC method, 30 MLs of CdS were initially grown on CdSe cores (CdSe30CdS), followed by thermal annealing at 280 °C for 4 h to minimize defects.[53,54] A portion of the CdSe30CdS QD batch was then taken into a new reaction flask, to which 20 MLs of CdS were added, followed by thermal annealing at 280 °C for 4 h to achieve CdSe50CdS. Similarly, CdSe80CdS QDs were synthesized from CdSe50CdS, and CdSe100CdS were synthesized from CdSe80CdS. The injection rate was set at 3 mL/h for all syntheses to maintain the growth of large, monodisperse particles.[40,55] In contrast to the syntheses of hexagonal pyramidal and bipyramidal CdSe/CdS QDs by Tan et al.,[52] purification between steps was not performed to allow more accurate calculations of the additional precursor amounts for the targeted number of CdS MLs based on the initial core concentration.

Figure 1b–j presents transmission electron microscopy (TEM) images of the CdSe cores and the resultant core/shell QDs, with their relative size distribution as bar graphs. TEM images show that CdSe30CdS QDs have hexagonal projections with sharp corners and flat facets, CdSe50CdS QDs have rounded projections, while the projections of CdSe80CdS and CdSe100CdS QDs are similarly diamond-shaped (the projection distribution for each sample is shown in Table S1 in the Supporting Information). The QDs with 30, 50, 80, and 100 CdS MLs have average sizes of 26.3 ± 2.2, 43.8 ± 4.2, 69.7 ± 6.5, and 92.4 ± 8.8 nm, respectively, showing a consistent size distribution where the variance does not exceed 10% of the mean size. Table 1 compares the targeted and measured diameters and the number of CdS MLs. The accuracy of size calculations decreases with increasing particle size due to the discrepancy between the spherical particle shape assumption used in the calculations and the actual particle shape.

Table 1. Summary of Targeted and Measured Particle Diameters and Number of CdS MLs[a]

samples	targeted diameter (nm)	measured size (nm)	targeted number of MLs	measured number of MLs
CdSe30CdS	23.75	26.3 ± 2.2	30	33.8 ± 3.3
CdSe50CdS	37.25	43.8 ± 4.2	50	59.7 ± 6.2
CdSe80CdS	57.50	69.7 ± 6.5	80	95.0 ± 8.9
CdSe100CdS	71.00	92.4 ± 8.8	100	126.1 ± 12.7

[a]For CdSe80CdS and CdSe100CdS, the listed measured sizes are averages of the diagonal and slant height. The number of MLs is calculated using 3.5 nm for the core diameter and 0.3375 nm for the thickness of one ML. For CdSe80CdS and CdSe100CdS, the number of MLs is calculated based on their shorter dimensions.

To validate the importance of the stepwise approach, we conducted a series of direct CdS shelling experiments. Without the stepwise approach, direct synthesis with identical conditions yielded similar particle shapes and sizes only up to 30 CdS MLs (Figure S11). However, attempts to shell CdSe cores directly with 40 and 50 CdS MLs resulted in a significant amount of twinning, particle instability, and a high level of polydispersity (Figure S11). This decline in structural integrity can be attributed to the accumulation of unreacted precursors, byproducts, and defects in the shell and at the core–shell interface.[52,53]

Following the synthesis of CdSe100CdS QDs using the stepwise shelling strategy, we added calculated amounts of Cd and S precursors to achieve CdSe115CdS (Figure 2a, top). However, we observed particle instability (Figure 2b). We hypothesize that this instability stems from the formation of

https://doi.org/10.1021/acsnano.4c06961
ACS Nano 2024, 18, 20726–20739

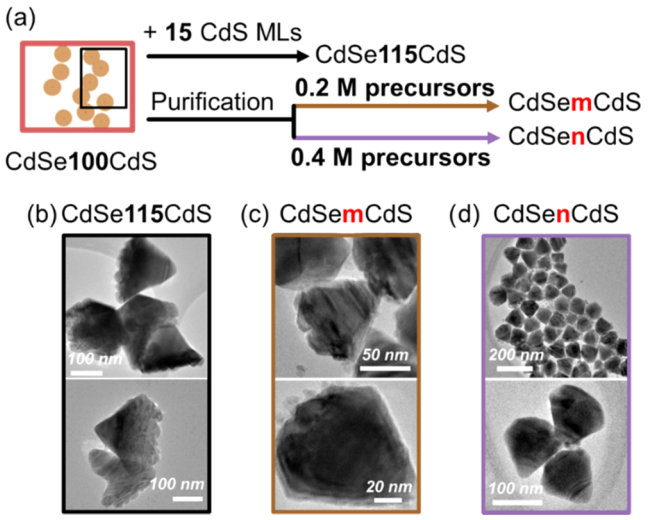

Figure 2. (a) Synthesis scheme for shelling beyond 100 MLs of CdS from CdSe100CdS. TEM images of resultant core/shell CdSe/CdS QDs with 115 (b), m (c), and n (d) CdS MLs, where m and n are arbitrary numbers of CdS MLs since determination of CdSe100CdS concentration after purification is not possible.

islands on a specific particle facet during the shelling process. Quantitative analysis revealed that 31% of the particles in the CdSe100CdS sample already exhibit island formations (appearing as distinct lumps in the TEM images) exclusively at the base of diamond-shaped projections, the (0001) facet. As known in the literature, the Cd-terminated facets of CdS nanocrystals have higher surface energy than other facets.[56,57] For CdSe100CdS QDs, the large surface area can be substantial enough to facilitate the formation of CdS islands and their subsequent independent growth into larger islands before a new ML uniformly covers the facet. Compared to flat facets, these large islands may generate more considerable surface strain, leading to instability or deformation of the particles at this facet.[58] Additionally, the formation of small nanorods was observed following this shelling step (Figure S10). This is attributed to the gradual dilution of the reaction solution after each step in the stepwise shelling process, which eventually favors the independent nucleation of small particles over shell growth on existing QD seeds. Thus, a higher deposition rate of the precursors and a more concentrated solution are required to achieve uniform deposition of additional shells onto all facets without promoting significant island growth on Cd-rich facets. We carried out two shelling experiments using the same molar amounts of precursors but different concentrations with purified and more concentrated solutions of CdSe100CdS QDs (Figure 2a, bottom). Compared with the shelling of a diluted particle sample, minimal particle instability was observed when 0.2 M precursor solutions were used (Figure 2c). A total of 95%, or 698 out of 725 particles counted, showed islands at the base of the diamond-shaped particles compared to 31% (142/459) for the CdSe100CdS sample (Figure S12). The hexagon base diagonal and the slant height of the resulting particles increased to 98.6 ± 7.4 and 103.8 ± 7.6 nm, respectively. Conversely, using 0.4 M precursor solutions resulted in almost no islands at the base of the diamond-shaped particles, with more small particles adhering to the large particles (Figure 2d). The diagonal of the hexagon base and the slant height of the resulting particles increased to 95.2 ± 6.5 and 98.5 ± 7.1 nm, respectively. Only 11% or 62 out of 565 counted particles displayed rough surfaces (Figure S12). Additionally, more small nanoparticles were observed around the large particles in this sample, attributed to the higher concentration of the added precursor solutions, which leads to increased independent nucleation and less material being deposited onto the seeds, leading to smaller resulting particles compared to those produced by using the 0.2 M precursor solutions. While it has been demonstrated that CdS particles larger than 200 nm can be synthesized, these methods require the use of highly polar solvent[56] or autoclaves,[59] and the particles produced from these methods are not colloidally stable. Such conditions can undermine the stability of the emissive CdSe cores for shelling. Meanwhile, our findings indicate that growing particles larger than our CdSe100CdS QDs with the current method and conditions becomes increasingly challenging due to complications associated with the relative concentration of precursors and the reaction solution.

Structural Characterization of Colossal QDs. *Shape Analysis and Facet Determination.* Since TEM images only show the particles from one projection, it is ambiguous whether the sample consists of a single-particle morphology observed from many different orientations or is a mixture of different morphologies (Table S1). To characterize the three-dimensional (3D) shape of the colossal NCs, we performed electron tomography in scanning transmission electron microscopy (STEM) mode on CdSe80CdS and CdSe100CdS QDs. Electron tomography involves acquiring a series of high-angle annular dark-field (HAADF) STEM images of the sample at different tilt angles. This approach allows the same particles to be imaged from multiple orientations. Utilizing the monotonic relationship between the HAADF intensity and projected thickness, the 3D shape of the particles can be reconstructed by processing this series of images. Specifically, we collected roughly 70 images per series from approximately −70 to 70° in 2° increments. The tilt series data was processed as described in Section S7 in the Supporting Information. Figure 3 shows the tomographic reconstruction of CdSe80CdS and CdSe100CdS QDs, both of which have diamond shapes. This diamond shape resembles the hexagonal pyramidal and bipyramidal CdSe/CdS nanocrystals studied by Tan et al.,[52] who determined the shape to be defined by (0001) and {10$\bar{1}$1}

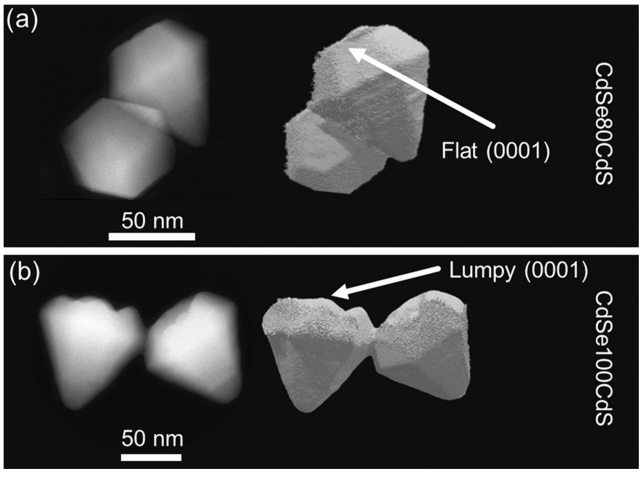

Figure 3. (a) Left: One image from the tilt series of CdSe80CdS QDs. Right: Reconstructed tomogram of two CdSe80CdS QDs. (b) Tilt series and a tomogram of two CdSe100CdS QDs.

https://doi.org/10.1021/acsnano.4c06961
ACS Nano 2024, 18, 20726−20739

facets stabilized by phosphonic acid and oleate ligands, respectively. However, unlike the pyramidal nanocrystals, defined by 6 $\{10\bar{1}1\}$ facets and one (0001) facet, or the bipyramidal nanocrystals, defined by 12 $\{10\bar{1}1\}$ facets, the diamond shape we observe appears to be a combination of both cases, being composed of 12 semipolar $\{10\bar{1}1\}$ facets and one polar (0001) facet. This hypothesis was tested with structural modeling in the software VESTA,[60] where we found that the shape of the colossal CdSe/CdS QDs in this study could be approximated by a combination of $\{10\bar{1}1\}$ facets and one (0001) facet. We suspect that the reason there is only one (0001) facet, as opposed to symmetric (0001) and $(000\bar{1})$ facets, is that the particle grows faster in the $[000\bar{1}]$ direction than the [0001] direction as predicted theoretically[61] and observed in wurtzite CdSe nanorods.[52,62]

The CdSe80CdS QDs exhibit flat faceting and closely resemble the modeled structure, albeit with some variation in the dimensions and relative size of the facets, as seen in the tilt series snapshots shown in Figure S16. The CdSe100CdS QDs studied show some deviations from the diamond shape, most notably lumps or ridges at the (0001) facet, as discussed above, which are resolved by TEM (Figure 1f) and STEM (Figures 3 and S16). Overall, tilt series information from multiple particles suggests that while there can be some variation in the dimensions of the particles, the morphology is consistent, defined by semipolar $\{10\bar{1}1\}$ faceting and asymmetric growth on the *c*-axis, leading to a pointy end in the $[000\bar{1}]$ direction and a flat (0001) facet.

In the study by Tan et al.,[52] small hexagonal pyramidal core/shell CdSe/CdS particles evolved into a larger, symmetrical hexagonal bipyramidal morphology upon further shelling after purification and the addition of oleylamine to completely remove octadecylphosphonic acid (ODPA) ligands. When more ODPA was added during the shelling of the hexagonal pyramidal CdSe/CdS particles, a large hexagonal pyramidal morphology was formed.[52] In our study, we propose that residual ODPA ligands from the CdSe cores remain strongly bound to the QDs. Coordination of ODPA to the CdSe cores and core/shell QDs was confirmed by ^{31}P NMR spectroscopy (Figure S21). This interaction leads to asymmetric shelling in the early stages of the sequential shelling process. As no more ODPA is added, it is significantly diluted at later shelling stages, culminating in a diamond morphology instead of hexagonal pyramidal or bipyramidal morphologies. Together with observations from Tan et al.[52] and Bladt et al.,[41] our results contribute to the library of giant QD morphologies and show that these shapes can be engineered by tuning shelling conditions (Figure 4). Additionally, the final diamond shape of our particles is similar to large CdS particles grown in polar solvents[56] or autoclave synthesis.[59]

To examine the morphology and crystal structure of our colossal QDs in greater detail, we performed STEM-HAADF imaging with an atomic resolution. Figure 5 shows CdSe9CdS (obtained by extracting an aliquot during the CdSe30CdS QD synthesis), CdSe30CdS, and CdSe50CdS QDs oriented down well-defined crystallographic directions. The particles are oriented parallel to the [0001] and [1100] directions of the crystal structure, as depicted by the VESTA models. The faceting of these particles from these crystallographic orientations is consistent with the diamond shape from Figure 3 and supports our characterization of the diamond shape as consisting of 12 $\{10\bar{1}1\}$ facets and one (0001) facet. The image of the CdSe9CdS sample matches well with the

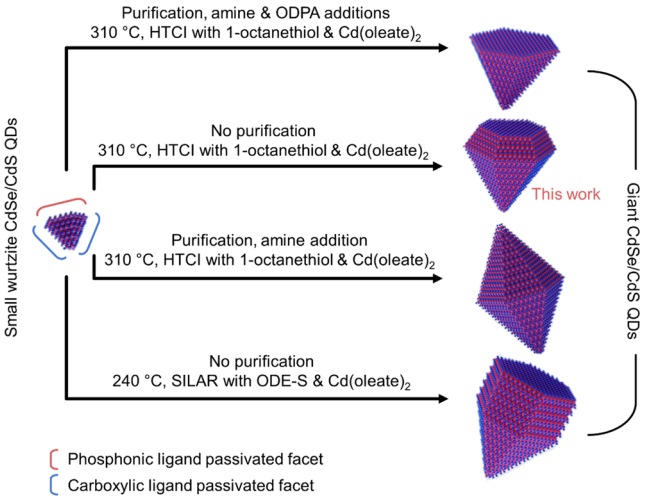

Figure 4. Shape evolution from small to giant wurtzite CdSe/CdS QDs is governed by shelling conditions. With seed purification and the addition of ODPA and amine, the HTCl method with 1-octanethiol and Cd(oleate)$_2$ yielded giant hexagonal pyramids (a). Without purification between shelling steps, the HTCl method with 1-octanethiol and Cd(oleate)$_2$ results in diamond giant QDs (b), while the addition of amine and the SILAR method with ODE-S and Cd(oleate)$_2$ results in bullet shape QDs (c). With purification between shelling steps and amine addition, the HTCl method with 1-octanethiol and Cd(oleate)$_2$ results in hexagonal bipyramidal giant QDs (d).

structural model. In contrast, in the case of CdSe30CdS and CdSe50CdS, we observe deviations from the model structures, which we interpret as evidence of stacking faults along the *c*-axis. Stacking faults can be observed directly in the magnified HAADF image in Figure 5f. We concluded that the appearance of faint atomic columns in the center of the hexagons in the magnified HAADF image in Figure 5e is due to the same type of stacking faults, as discussed in detail in Section S7. The observation of stacking faults in the CdSe30CdS and CdSe50CdS QDs but not in the CdSe9CdS QDs suggests that stacking faults become more common as the shell thickness increases. The stacking faults appear to be relatively concentrated in the shorter [0001] growth direction (Figure S17), consistent with observations of asymmetric concentrations of stacking faults in CdSe nanorods.[62] The asymmetric concentration of stacking faults may also describe patterns observed in the CdSe30CdS QDs oriented down the [0001] direction, as described in more detail in Figures S18 and S19. Asymmetric growth is also observed in Figure 5a, where the shape is nominally hexagonal but some faces are smaller than others. This reduces the symmetry of the structure from 6-fold rotational symmetry to 3-fold rotational symmetry. Overall, atomic resolution STEM-HAADF imaging suggests that colossal CdSe/CdS QDs feature a diamond morphology, with some asymmetry in the growth of the facets.

Given the somewhat asymmetric growth of the CdS shell, it is worth examining whether the CdSe core is placed in the center of the core/shell structure or biased toward one end. To characterize the position of the CdSe core, we performed energy dispersive X-ray spectroscopy (EDS) in a scanning transmission electron microscope on CdSe9CdS QDs. CdSe9CdS was selected because the shell is thin enough to detect EDS signal from the CdSe core yet large enough to remain sufficiently stable under the electron beam.[40] Visual

https://doi.org/10.1021/acsnano.4c06961
ACS Nano 2024, 18, 20726−20739

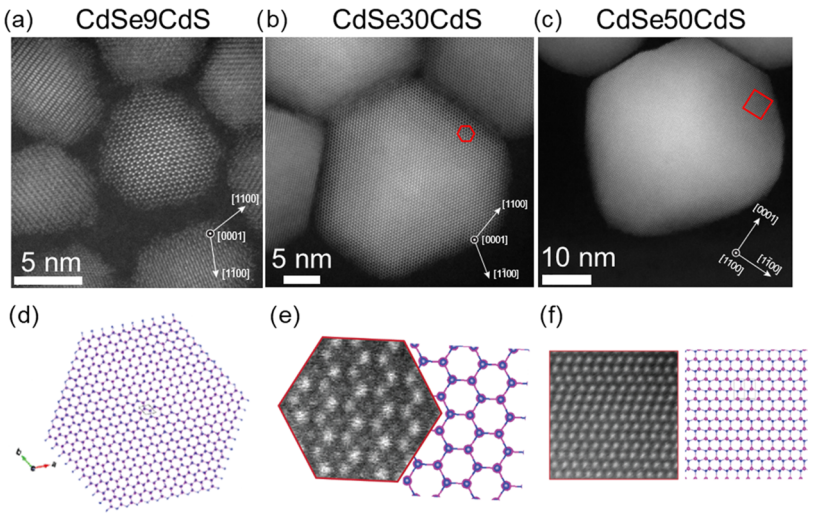

Figure 5. Atomic resolution HAADF-STEM images of (a) CdSe9CdS and (b) CdSe30CdS oriented looking down the [0001] direction and (c) CdSe50CdS oriented down the [1100] direction. (d–f) Structural models generated in VESTA reveal that the atomic structures largely match the expected structure from these orientations. For the thicker shell samples, deviations such as the faint columns in the center of the hexagons in (e) and stacking faults in (f) are observed.

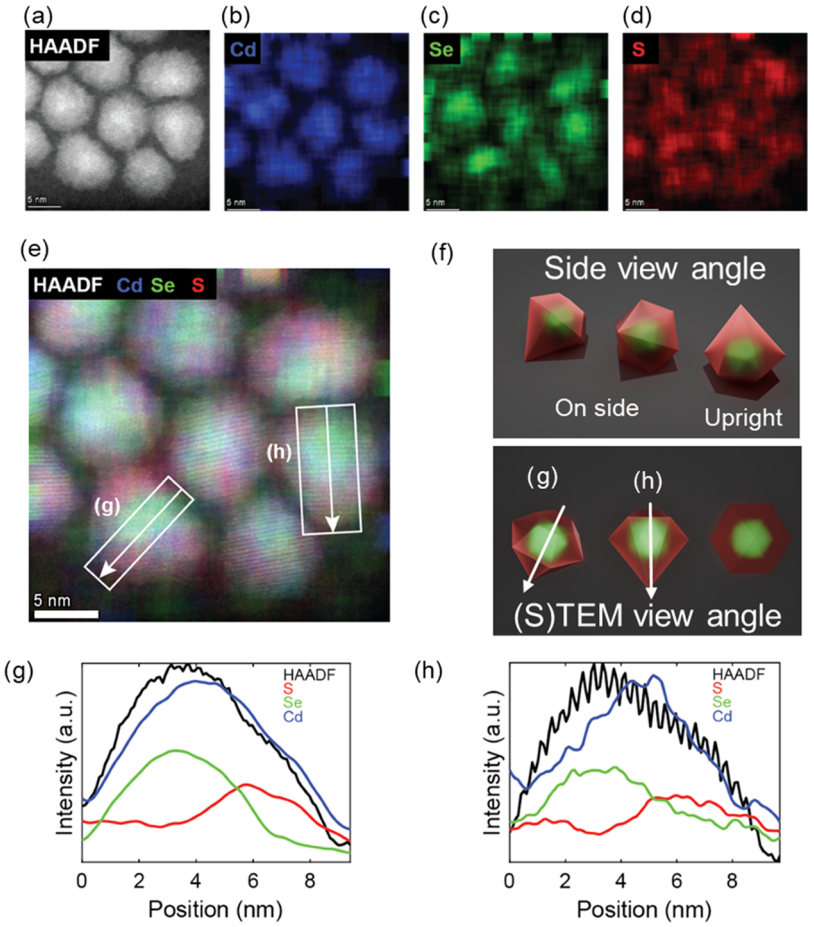

Figure 6. STEM-EDS of CdSe9CdS NCs. (a–d) Isolated HAADF image and Cd, Se, and S compositional maps. (e) Overlay of HAADF with Cd, Se, and S composition maps. Cd, Se, and S signal is averaged to resolve structures more easily. (f) Schematic of particles illustrating core/shell structure from different orientations. (g, h) Line profiles showing HAADF and EDS intensity as a function of position for two particles in (e). To improve the signal-to-noise ratio, the EDS signal was averaged over 28 pixels (2.83 nm).

inspection of the EDS composition maps in Figure 6b–d, as well as line profiles drawn through two particles (Figure 6e,g,h), reveals that the CdSe cores are located toward one end of the particle. This is consistent with the asymmetric growth of the CdS shell, which causes the CdSe core to be closer to

https://doi.org/10.1021/acsnano.4c06961
ACS Nano 2024, 18, 20726–20739

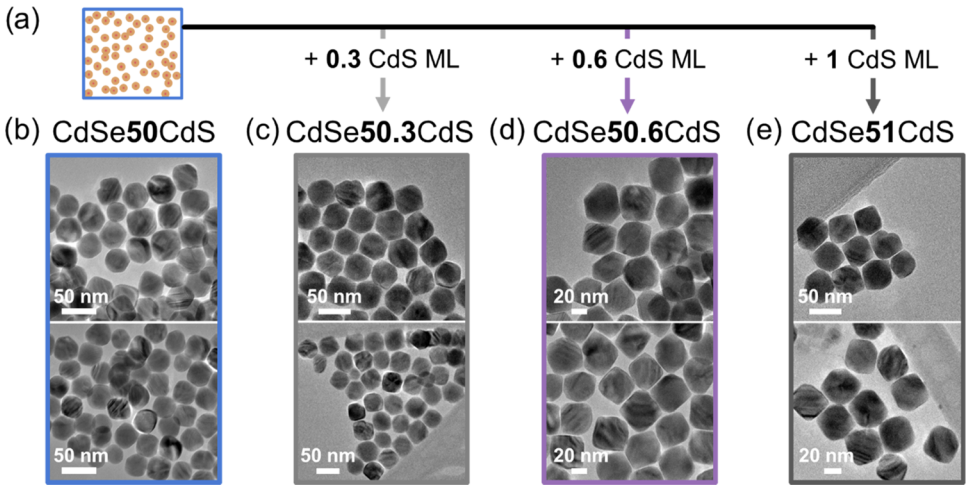

Figure 7. TEM images of CdSe50CdS (a) and the products from flat facet reconstruction achieved by the addition of 0.3 (b), 0.6 (c), and 1 (d) ML of CdS.

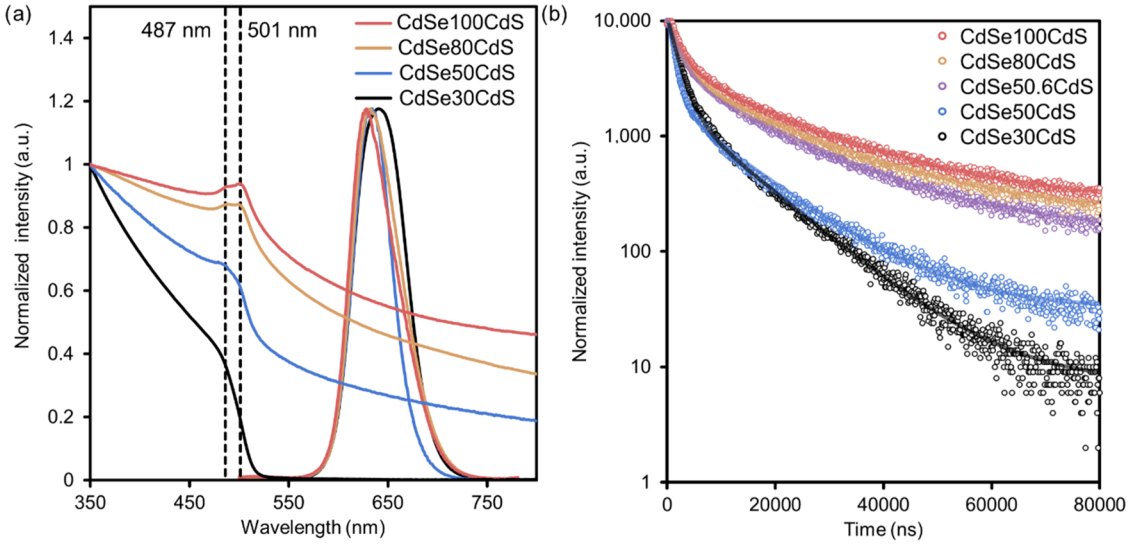

Figure 8. Solution-phase absorption and PL spectra (a) and time-resolved PL decay (b) of CdSe30CdS (black), CdSe50CdS (blue), CdSe50.6CdS (purple), CdSe80CdS (yellow), and CdSe100CdS (red) QDs with an excitation wavelength of 525 nm. All data were collected after one centrifugation step with methyl acetate as an antisolvent and hexane as a solvent without size-selective purification.

the slower-growing (0001) facet rather than the faster-growing tip in the [000$\bar{1}$] direction (Figure 6f).

Structural Rounding and Flat Facet Reconstruction. As seen in the TEM images (Figure 1b–f), all syntheses consistently yielded particles with sharp corners, except for the CdSe50CdS QDs (Figures 1d and 5c). Despite all samples in this synthesis series undergoing thermal annealing at high temperatures for several hours after their synthesis, only the CdSe50CdS batch shows rounded facets. Recent studies have revealed that the conversion from faceted CdSe/CdS nanocrystals to their spherical counterparts is independent of particle size[63] and can be driven by factors such as increased annealing temperature and duration,[52,53,64] high concentrations of amine ligands,[52,57,65,66] and selective facet-ligand pairing.[57] In our study, all syntheses included an identical annealing step (280 °C for 4–6h) without adding extra phosphonic acids or amines, yet both faceted and spherical particles were observed in different batches (Figures 1d and S15). Since spherical particles appeared without any deliberate chemistry to induce facet reconstruction, this rounding is likely due to the incomplete formation of CdS MLs on the seeds, followed by atom migration facilitated by the high annealing temperatures. When large particles are shelled, adding an extra ML requires a significant amount of Cd and S atoms to be deposited uniformly onto the particle seed. If the reaction is stopped prematurely or the precursor supply is depleted before a growing ML is complete, subsequent annealing can lead to intraparticle atom migration, resulting in ripening of sharp edges and corners and the formation of thermodynamically favorable rounded particles. Interestingly, this transformation is reversible during the sequential shelling, as demonstrated by the evolution from CdSe50CdS to CdSe80CdS (Figure 1d–e). We confirmed this reversibility through a series of experiments where a submonolayer of CdS was added to the rounded CdSe50CdS particles (Figure 7a). TEM images of the resulting particles, Figure 7c–e, reveal structures with more flat facets and sharper corners than the initially rounded particles (Figure 7b). We used the circularity index (C) to quantitatively assess the roundness of the particle shapes. This index ranges from 0.70 to 0.86 for diamond-like or truncated kite two-

https://doi.org/10.1021/acsnano.4c06961
ACS Nano 2024, 18, 20726–20739

Table 2. Summary of PLQY of As-Synthesized QDs, QDs Stored under Ambient Conditions after 4 Months, and Their Lifetimes (Excited at 525 nm) Derived from Biexponential Fits of Time-Resolved PL Decays

samples	PLQY as-synthesis (%)	PLQY after 4 months in air (%)	t_1 (μs)	A_1	t_2 (μs)	A_2	t_{av} (μs)
CdSe30CdS	36.8 ± 1.2	34.3 ± 0.7	1.72 ± 0.01	8.44 ± 0.04	10.18 ± 0.15	2.16 ± 0.04	3.45 ± 0.08
CdSe50CdS	30.9 ± 0.8	30.3 ± 0.6	1.21 ± 0.01	8.69 ± 0.04	11.10 ± 0.19	1.90 ± 0.03	2.98 ± 0.08
CdSe50.6CdS	28.1 ± 0.4	27.6 ± 0.8	3.34 ± 0.02	3.34 ± 0.02	15.06 ± 0.15	1.78 ± 0.02	6.54 ± 0.08
CdSe80CdS	15.8 ± 1.0	15.1 ± 0.8	1.90 ± 0.02	3.26 ± 0.02	16.03 ± 0.16	1.79 ± 0.01	6.91 ± 0.08
CdSe100CdS	10.5 ± 0.6	11.2 ± 1.1	2.99 ± 0.02	2.98 ± 0.02	17.00 ± 0.15	1.96 ± 0.01	7.93 ± 0.07

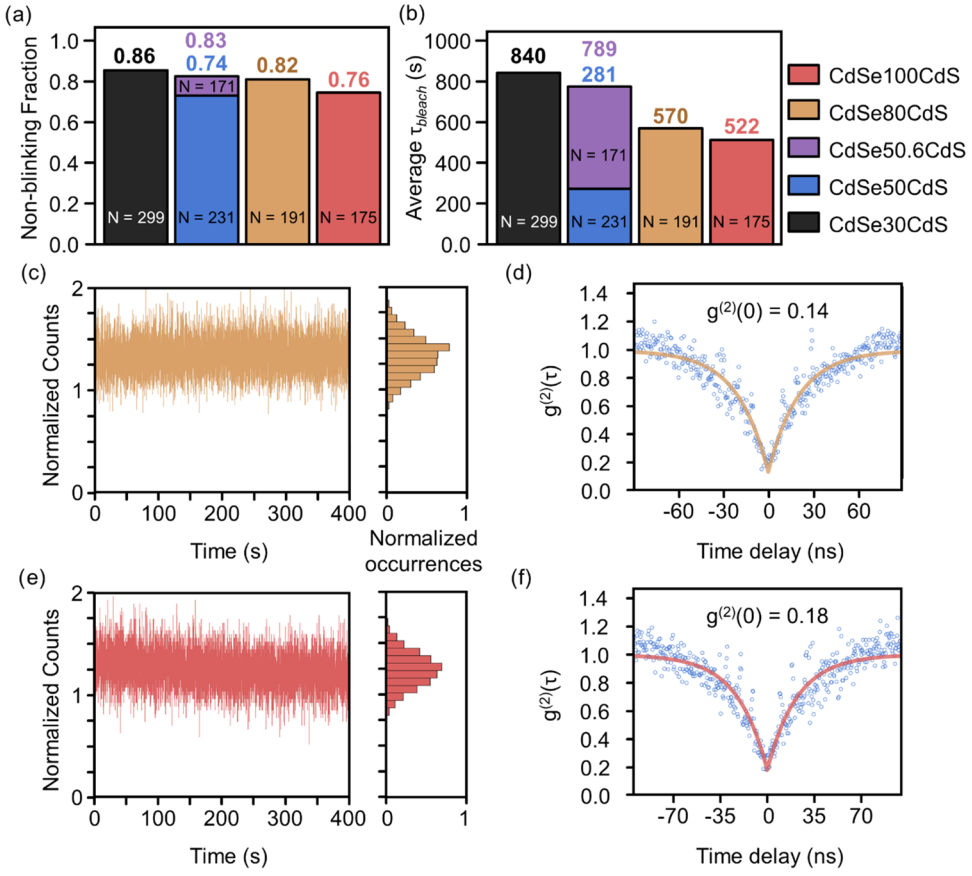

Figure 9. Nonblinking fractions (a) and average photobleaching time constant (b) of colossal QDs. Representative PL traces (c, e) and second-order autocorrelation function $g^{(2)}(\tau)$ (d, f) from single CdSe80CdS and CdSe100CdS QDs.

dimensional (2D) projections, indicating less rounded shapes, and exceeds 0.9 for hexagonal projections, with values approaching 1.0 as the shapes become more circular (Section S5). We only applied this measurement to the diamond-like projections to avoid overestimating circularity. Adding less than one CdS ML did not significantly change the overall sizes of the particles but resulted in a noticeable decrease in their C values from 0.84 ± 0.03 to less than 0.80 (Figure S14).

Optical Properties of Colossal QDs. The ensemble normalized optical absorption and emission spectra of the colossal QD series taken in anhydrous hexane are shown in Figure 8a. The CdSe30CdS QDs show typical absorption features for giant CdSe/CdS QDs, where absorption is dominated by the CdS shell, and onset happens around the bulk CdS bandgap energy, 515 nm. The absorption feature of the larger QDs is similar to that of bulk CdS particles (Figure S22). As the CdS shell thickness and overall particle size increase, significant scattering becomes evident across the visible region and two distinct absorption peaks arise at 487 and 501 nm. Deciphering the origin of these features requires deconvolution of the contributions from absorption, scattering, and refraction, a process that presents significant complexity.[67,68] The emission peaks (Figure 8a) of the colossal QDs exhibit a slight blue shift from 642 to 629 nm, likely due to ionic intradiffusion,[69−71] and a line width narrowing as the number of CdS monolayers increases. The photoluminescence quantum yields (PLQYs) for all samples are detailed in Table 2, indicating a gradual decrease from 36.8% for CdSe30CdS to 10.5% for CdSe100CdS. Due to significant scattering of the solutions, these values represent a lower bound due to overestimation of the number of photons absorbed by the sample.[72] Even after 4 months of storage in hexane under ambient conditions, the PLQYs remained stable (Table 2).

Figure 8b presents the time-resolved PL decay traces of the QDs at room temperature, and Table 2 lists the decay times derived from biexponential fits, showing average lifetimes of a few microseconds for all samples. These long lifetimes and their correlation with shell thickness are consistent with our understanding that the electron wave function delocalizes into the shell volume in this core−shell system. This delocalization

https://doi.org/10.1021/acsnano.4c06961
ACS Nano 2024, 18, 20726−20739

reduces the overlap between electron and hole wave functions, increasing the radiative lifetime.[45,73] Compared to giant QDs with smaller sizes reported in the literature to date, the lifetimes of these colossal QDs are longer (Table S3), suggesting that the increase in wave function separation with shell thickness has not yet reached a maximum.

Interestingly, the CdSe50CdS QDs with rounded edges have shorter photoluminescence lifetimes (~3 μs), which deviate from the expected trend seen in other samples. In contrast, CdSe50.6CdS QDs with flat facets exhibit significantly longer lifetimes (~6 μs). This observation suggests that subtle changes in particle morphology and surface structure, even in this size regime, can directly and substantially affect the optical properties. Since the primary distinction between the CdSe50CdS and CdSe50.6CdS QDs lies in their surface morphology, we believe that surface strain is a critical parameter. As discussed previously, the rounded facets likely result from surface reconstruction due to an incomplete monolayer, thereby inducing strain similar to that observed in flat and helical ZnS shells of ZnSe/ZnS nanorods[58] (Section S10).

To evaluate the blinking behavior of single colossal QDs, we used wide-field PL microscopy to sample hundreds of single QDs. Figure 9a illustrates the nonblinking fractions across the samples (more details in Section S14), with all QDs in the series showing significant nonblinking behavior, typical for thick-shelled CdSe/CdS. To assess QD photobleaching, each single-particle PL trace was fit to a single exponential equation:[74]

$$I(t) = Ae^{-t/\tau_{bleach}} \quad (1)$$

where τ_{bleach} is the characteristic time of the QD photobleach and A is an intensity-related prefactor. As the shell thickness increases, the average photobleaching time decreases, with the rounded QDs exhibiting faster bleaching than the similarly sized flat-faceted QDs (Figure 9b). Our wide-field PL analysis indicates that there is no definitive trend in blinking behavior as shell thickness increases, despite Figure 9a suggesting a decrease in the nonblinking fraction. This is because "blinking" fractions for the larger QDs are primarily reporting on photobleached QDs. Furthermore, single-particle PL comparisons reveal that flat-faceted CdSe50.6CdS QDs exhibit a clearly improved nonblinking fraction and longer photobleaching time compared to the rounded CdSe50CdS QDs (Figure 9a,b). This distinction highlights the impact of facet morphology on the QD performance.

Single-particle PL traces of all colossal QDs showed a stable PL intensity with a unimodal ON state over many minutes of measurement under excitation. Figure 9c,e shows representative PL traces of a single QD with 80 and 100 CdS ML, respectively. To assess the single-photon emission of colossal QDs, we measured the second-order temporal correlation function ($g^{(2)}(\tau)$) of many single QDs. All measured single QDs, regardless of shell thickness, have a $g^{(2)}(0) < 0.4$, which is indicative of a single-photon emitter under continuous-wave excitation without any spectral filtering or background correction. Figure 9d,f presents $g^{(2)}(\tau)$ curves of CdSe80CdS and CdSe100CdS single QDs, respectively, with $g^{(2)}(0)$ values below 0.2. In contrast, giant CdSe/CdS QDs with much smaller sizes have been reported with $g^{(2)}(0)$ values above 0.3.[48,75] Given that thick CdS shells can efficiently promote recombination of stable multiexcitons[42,48] that are believed to potentially affect the single-photon emission purity, our results imply that this factor either does not scale proportionally with the thickness of the CdS shell or has minimal impact on the single-photon emission from CdSe/CdS QDs.

Compared to the previously reported giant CdSe/CdS QDs (Table 3), colossal QDs are poised to be highly effective for scalable and deterministic single-particle positioning and ultimately precise coupling with optical cavities using solution-processable techniques, including template-assisted self-assembly,[17] electrohydrodynamic inkjet printing,[76,77] and those that have been used for other particles with sub-100 nm diameters.[78]

Table 3. Feature Comparison of CdSe/CdS with Different Shell Thickness Regimes

features	thin shells	thick shells	colossal shells
number of CdS MLs	5−10	10−30	30−100
diameter	<10 nm	10−20 nm	20−100 nm
PLQY	>90%[49,53]	<90%[39,40]	<50%
emission lifetime	<100 ns	100 ns −1 μs	>1 μs
blinking	significant	highly suppressed	highly suppressed
colloidal stability	high	high	moderate
single-particle positioning	random	random	large scale and deterministic*

*Large-scale deterministic positioning has been shown for particles with size from 50 to 100 nm.[17,79,80]

CONCLUSIONS

In summary, we have demonstrated that a stepwise HTCI method is essential for synthesizing colossal core−shell CdSe/CdS QDs with diameters of up to 100 nm and size distributions under 10%. This is in contrast to more conventional direct shelling to prepare core/shell QDs of over 50 nm in diameter, which results in instability and independent CdS nucleation. Additionally, pushing the QD size above 100 nm requires careful adjustment of the precursor concentrations. These colossal QDs display a hexagonal diamond shape with the CdSe core situated closer to the particle base. Structural analysis through microscopic techniques confirmed that the particles consist of 12 semipolar $\{10\bar{1}1\}$ facets and one polar (0001) facet. Our observations also revealed that particle rounding occurs during shelling due to incomplete monolayer growth. These rounded QDs can be sharpened by introducing a small amount of shelling precursors to complete the CdS ML.

We have shown that with a significantly large number of CdS shells, the optical properties of colossal QDs remain similar to those of previously reported giant QDs with diameters <20 nm. Additionally, we have confirmed that QD surface morphology can directly affect optical properties, and this could only be observed clearly in the colossal particle size regime. All samples of colossal QDs in this study exhibit long solution-phase PL lifetimes of a few microseconds at room temperature, consistently demonstrate nonblinking fractions above 70%, and maintain low antibunching emission even for QDs with 100 MLs of CdS. The optical properties differ markedly between rounded and flat-faceted particles, with the latter showing enhanced PL lifetime and improved nonblinking behavior.

Our findings regarding particle morphologies and properties throughout the shelling process in this colossal particle size

https://doi.org/10.1021/acsnano.4c06961
ACS Nano 2024, 18, 20726−20739

regime provide valuable insights into precision for crystal growth and size-dependent optical properties. We believe that this synthetic approach will unlock numerous innovative applications for QDs and represents a crucial step toward the practical development of real optoelectronic devices, especially those utilizing single-QD emitters.

EXPERIMENTAL METHODS

Materials. All chemicals listed below were used without further purification, unless stated otherwise. Oleic acid (≥90%), anhydrous methyl acetate (99.5%), selenium powder (99.999%, 100 mesh), cadmium oxide powder (CdO, 99.9%), trioctylphosphine oxide (TOPO, 99%), trioctylphosphine (TOP, 90%), 1-octanethiol (99%), 1-octadecene (ODE, 90%), and anhydrous hexane (95%) were purchased from MilliporeSigma, and n-octadecylphosphonic acid (ODPA, 99%) was purchased from PCI Synthesis. Cadmium oleate was synthesized following a literature procedure.[49]

Synthesis. *Wurtzite CdSe QDs.* Wurtzite CdSe QDs were synthesized using an established method with some minor modifications.[54] TOPO (3 g), CdO (0.06 g), ODPA (0.28 g), and a magnetic stir bar were loaded into a 15 mL three-neck round-bottom flask secured with a septum, a thermowell equipped with a thermometer, and a condenser. The flask was heated to 110 °C and put under a vacuum for 30 min. The flask was then refilled with N_2 gas and was heated to 375 °C. While the temperature was ramping up from 320 to 370 °C, TOP (1.5 mL) was added slowly into the reaction. When the temperature was stabilized around 372−375 °C, a solution of Se powder (0.058 g) completely dissolved in TOP (0.4 mL) was quickly injected into the reaction. The reaction temperature fluctuated around 368−370 °C. The heating was stopped 45 s after the Se injection. The flask was quickly cooled to room temperature with forced air to yield QDs with the lowest energy electronic transition at 560 nm. The product was purified in a glovebox with methyl acetate as antisolvent and hexane as solvent and was stored in a N_2 gas-filled glovebox. Using molar extinction coefficient and sizing curve estimations from the literature,[49,81] the particle diameter was calculated to be 3.5 nm and the concentration of the CdSe QDs in hexane was 1.00×10^{-4} M.

Direct Shelling of CdSe with CdS. ODE (6 mL) was added into a 25 mL three-neck round-bottom flask secured with a septum, a thermowell equipped with a thermometer, and a condenser. The flask was heated to 110 °C and put under a vacuum for 60 min. The flask was refilled with N_2 gas and a desired amount of CdSe core in hexane (typically 5−100 nmol of QD or 0.0048−0.96 mL of the solution) was added to the reaction solution. The reaction solution was put under vacuum for 30 min to remove all hexane and then was refilled with N_2 gas. The flask was heated to 310 °C. When the temperature was at 260 °C, 0.2 M $Cd(Oleate)_2$ and 0.2 M 1-octanethiol solutions with amounts calculated based on the CdSe core amount and the desired number of CdS ML or final size, both in ODE, were injected into the reaction flask using a dual-syringe pump with the rate of 3 mL/h. Usually, the temperature reaches 310 °C 5 min after injection starts. Calculations of precursor amounts are detailed in the Supporting Information. When the injection was completed, the reaction mixture was kept at 310 °C for 10 min and then at 280 °C for at least 2 h. The flask was quickly cooled to room temperature with forced air and was brought into a glovebox for purification with methyl acetate/hexane.

Stepwise Shelling of CdSe with CdS. The schematic stepwise shelling process for the samples in our study is described in Figure 1a. Initially, CdSe cores were shelled with 30 monolayers (MLs) of CdS using the direct shelling method outlined previously. After the reaction was cooled to 85 °C, a portion of the reaction was transferred to a separate N_2 gas-filled three-neck round-bottom flask, which was subsequently heated to 310 °C. This procedure was replicated to add an additional 30 CdS MLs, resulting in CdSe80CdS QDs, and once more to add 20 CdS MLs, resulting in CdSe100CdS QDs. The sample portions that were not used for stepwise shelling were brought into a glovebox for purification with methyl acetate/hexane and characterization.

Measurements. *(Scanning) Transmission Electron Microscopy ((S)TEM).* TEM imaging was done on an FEI Tecnai G2 F20 SuperTwin microscope operated at 200 kV by using bright field imaging. Samples were prepared in a nitrogen glovebox by drop-casting 5 μL of dilute QD suspensions in toluene onto a suspended ultrathin carbon film on a lacey carbon support film, 400 mesh, copper grids purchased from Ted Pella Inc., allowed to dry fully (10 min), and then placed under vacuum overnight. TEM size analysis, including size measurements and circularity index assessment, was performed using manual analysis in ImageJ over at least 150 particle diameter measurements per sample.

STEM was performed with a Thermo Scientific Titan Themis operated at an accelerating voltage of 300 kV. Samples were prepared by drop-casting solutions of the QDs onto TEM grids (Ted Pella, Prod#01824; ultrathin carbon film on lacey carbon support film, 400 mesh, Cu). Samples were dried under a vacuum. Excess ligands were removed from the CdSe50CdS, CdSe80CdS, and CdSe100CdS samples by submerging the grids in ethanol over activated carbon, adapting a procedure from Li et al.[82] Prior to imaging, samples were further dried under a vacuum at 120 °C overnight. Energy dispersive X-ray spectroscopy (EDS) was performed with a Super-X quad EDS detector. Tilt series were acquired from roughly −70 to 70° using a Gatan Elsa Cryo-Transfer Holder with an ultralow-profile tip at room temperature. To accommodate a wide range of angles for the tilt series, the samples were drop-cast onto 200 mesh TEM grids (Ted Pella, Prod no. 01841; carbon film on 200 mesh, Cu). Samples were cleaned by the same process as that described before.

STEM Analysis. EDS analysis was performed with Thermo Scientific Velox software.

Tilt series images were aligned in ImageJ using the TomoJ plugin.[83] The aligned tilt series were cropped, and then tomographic reconstruction was performed with TomoJ. The resulting image stack was thresholded and exported using the 3D Viewer plugin and visualized in Microsoft PowerPoint.[84]

Analysis of atomic column intensity and position (Figure S18) was performed with StatSTEM.[85]

Model structures were constructed in VESTA.[60] To construct a model with stacking faults, as shown in Figure S19, the model was exported from VESTA into MATLAB. A stacking fault was induced by reflecting and shifting the coordinates of atoms in the outermost {0001} plane. Atoms outside of certain bounds were deleted to make a well-defined slab for easier comparison with other slabs.

Multislice STEM simulations were performed with the ab TEM Python Package.[86]

Solution UV−Visible Absorption and PL Measurements. Ultraviolet−visible (UV−vis) spectra were collected on a Cary 5000 spectrophotometer from Agilent. Steady-state PL measurements were taken on a HORIBA Jobin Yvon FluoroMax-4 fluorescence spectrophotometer, and quantum yield measurements were taken with a Hamamatsu C9920−12 integrating sphere with a Hamamatsu C10027−01 photonic multichannel analyzer. All PLQY measurements were taken in triplicate. Time-resolved photoluminescence decay was measured using an Edinburgh FLS 1000 Fluorimeter located in the University of Washington's MEM-C shared user facility. The excitation wavelength is 525 nm.

Single-Particle PL, Wide-Field PL, and $g^{(2)}$ Measurements. Low fluorescence glass coverslips (VistaVision#1.5 22 mm × 22 mm, VWR) were cleaned via sequential sonication in soap solution, deionized water (×2), acetone, and IPA with each sonication lasting 10 min. Immediately prior to sample deposition, each side of the coverslips was UV-ozone cleaned for 23 min.

Low-concentration QD solutions were prepared in hexanes via serial dilution. The solutions were diluted by a factor of 1000 to 100,000 and sonicated for 10 min. Single-QD films were then prepared via spin coating. 60 μL of solution was deposited onto the cleaned coverslips and spun at 2000 rpm for 40 s. The films were measured immediately after spin coating.

https://doi.org/10.1021/acsnano.4c06961
ACS Nano 2024, 18, 20726−20739

Wide-field microscopy measurements were performed on a Nikon TE2000 inverted optical microscope using a CFI Super Fluor 40× Oil immersion objective (NA = 1.3) with an Olympus F immersion oil. The illumination source was a 415 nm light-emitting diode (LED) (SOLIS-415C, Thor Laboratories) at a power density of 47 mW/cm^2. The following filters were used for the measurement: FF02−650/100 (AVR Optics), FF01−424/SP-25 (Semrock), and ZT488rdc (Chroma) mounted in Chroma Laser TIRF for Nikon TE2000/T filter cube. Videos of the sample photoluminescence over time were collected on a Prime 95B (Photometrics) camera. Videos consisted of 8000 images with an integration time of 50 ms. Individual QD photoluminescence traces were extracted from the videos using a custom-built Python package for selecting bright objects from a dark background and analyzed using a custom Python package for Change Point Analysis.[87,88] More details describing the Change Point Analysis and particle selection code and performance can be found elsewhere.[88] Our particle selection and CPA code is publicly available at: https://github.com/GingerLabUW/Widefield-CPA.

Single-particle spectroscopy was performed in ambient conditions with a home-built scanning PL setup. QDs were spin-coated on a Si/SiO_2 substrate. 532 nm continuous-wave laser light (Laserglow Technologies 532 nm DPSS Laser) was focused on the sample using a 100× (NA 0.95) dry objective lens. The typical excitation power was 5 μW as measured before the objective lens. The position of the excitation/collection spot was controlled by a fast-steering mirror (Newport FSM-300−01). The collected PL was filtered through a 580 nm long-pass filter and fiber-coupled either to a spectrometer to collect the PL spectrum or through a 50:50 fiber splitter to a pair of avalanche photodiodes MPD-plasma desorption mass (MPD-PDM) to collect the $g^{(2)}$ spectrum. For the $g^{(2)}$ spectra, the time correlation was performed by a time tagger (PicoQuant TimeHarp 260). The PL time traces were collected in parallel with the $g^{(2)}$ spectra. Custom software was used to map a specific area of the sample first and allow us to select specific spots for all measurements. PL counts were displayed live during the measurement. We considered emitters that appeared as isolated spots in the PL map and showed a PL count larger than 3000 and less than 50 k.

ASSOCIATED CONTENT

Supporting Information

The Supporting Information is available free of charge at https://pubs.acs.org/doi/10.1021/acsnano.4c06961.

Details of QD synthesis; additional (S)TEM and SEM images and analysis; X-ray diffraction patterns; and additional single-particle PL and $g^{(2)}$ traces (PDF)

Accession Codes

H.A.N., B.F.H., D.S., J.K., G.S., S.M.H., E.N., S.S., D.G., A.M., S.Y., G.D., B.M.C.C. Core/Shell CdSe/CdS Quantum Dot Emitters. 2024.ChemRxiv. DOI: 10.26434/chemrxiv-2024-md0hn (accessed July 3, 2024).

AUTHOR INFORMATION

Corresponding Author

Brandi M. Cossairt − *Department of Chemistry, University of Washington, Seattle, Washington 98195, United States;* orcid.org/0000-0002-9891-3259; Email: cossairt@uw.edu

Authors

Hao A. Nguyen − *Department of Chemistry, University of Washington, Seattle, Washington 98195, United States;* orcid.org/0000-0001-6742-1748

Benjamin F. Hammel − *Materials Science and Engineering, University of Colorado, Boulder, Colorado 80309-0215, United States;* orcid.org/0000-0002-9155-9875

David Sharp − *Department of Physics, University of Washington, Seattle, Washington 98195, United States;* orcid.org/0000-0002-1034-8567

Jessica Kline − *Department of Chemistry, University of Washington, Seattle, Washington 98195, United States;* orcid.org/0000-0002-2957-1160

Griffin Schwartz − *Department of Chemistry, University of Washington, Seattle, Washington 98195, United States*

Samantha Harvey − *Department of Chemistry, University of Washington, Seattle, Washington 98195, United States*

Emily Nishiwaki − *Department of Chemistry, University of Washington, Seattle, Washington 98195, United States;* orcid.org/0000-0002-3419-8604

Soren F. Sandeno − *Department of Chemistry, University of Washington, Seattle, Washington 98195, United States*

David S. Ginger − *Department of Chemistry, University of Washington, Seattle, Washington 98195, United States;* orcid.org/0000-0002-9759-5447

Arka Majumdar − *Department of Physics and Department of Electrical and Computer Engineering, University of Washington, Seattle, Washington 98195, United States;* orcid.org/0000-0003-0917-590X

Sadegh Yazdi − *Materials Science and Engineering, University of Colorado, Boulder, Colorado 80309-0215, United States; Renewable and Sustainable Energy Institute, University of Colorado, Boulder, Colorado 80309-0215, United States;* orcid.org/0000-0002-3470-9398

Gordana Dukovic − *Materials Science and Engineering, University of Colorado, Boulder, Colorado 80309-0215, United States; Department of Chemistry and Renewable and Sustainable Energy Institute, University of Colorado, Boulder, Colorado 80309-0215, United States;* orcid.org/0000-0001-5102-0958

Complete contact information is available at: https://pubs.acs.org/10.1021/acsnano.4c06961

Notes

The authors declare no competing financial interest.

ACKNOWLEDGMENTS

The authors thank Helen Larson for preliminary (S)TEM-EDS results. This work was supported by the National Science Foundation under Grant No. DMR-2019444. Part of this work was conducted at the Molecular Analysis Facility, a National Nanotechnology Coordinated Infrastructure site at the University of Washington, which is supported in part by funds from the National Science Foundation (awards NNCI-2025489, NNCI-1542101), the Molecular Engineering & Sciences Institute, and the Clean Energy Institute. Part of this work was conducted at the Facility for Electron Microscopy of Materials at the University of Colorado at Boulder (CU FEMM, RRID: SCR_019306). B.F.H. acknowledges support from the NSF through the Graduate Research Fellowship Program (NSF-GRFP) under grant no. DGE 2040434. S.M.H. acknowledges support from an appointment to the Intelligence Community Postdoctoral Research Fellowship Program at University of Washington administered by Oak Ridge Institute for Science and Education (ORISE) through an interagency agreement between the U.S. Department of Energy and the Office of the Director of National Intelligence (ODNI).

REFERENCES

(1) Aharonovich, I.; Englund, D.; Toth, M. Solid-State Single-Photon Emitters. *Nat. Photonics* **2016**, *10*, 631−641.
(2) Reimer, M. E.; Cher, C. The Quest for a Perfect Single-Photon Source. *Nat. Photonics* **2019**, *13*, 734−736.
(3) Zhong, H.-S.; Wang, H.; Deng, Y.-H.; Chen, M.-C.; Peng, L.-C.; Luo, Y.-H.; Qin, J.; Wu, D.; Ding, X.; Hu, Y.; et al. Quantum Computational Advantage Using Photons. *Science* **2020**, *370*, 1460−1463.
(4) Walker, T.; Kashanian, S. V.; Ward, T.; Keller, M. Improving the Indistinguishability of Single Photons from an Ion-Cavity System. *Phys. Rev. A* **2020**, *102*, No. 032616.
(5) Darquié, B.; Jones, M. P. A.; Dingjan, J.; Beugnon, J.; Bergamini, S.; Sortais, Y.; Messin, G.; Browaeys, A.; Grangier, P. Controlled Single-Photon Emission from a Single Trapped Two-Level Atom. *Science* **2005**, *309*, 454−456.
(6) Abe, N.; Mitsumori, Y.; Sadgrove, M.; Edamatsu, K. Dynamically Unpolarized Single-Photon Source in Diamond with Intrinsic Randomness. *Sci. Rep.* **2017**, *7*, No. 46722.
(7) Mizuochi, N.; Makino, T.; Kato, H.; Takeuchi, D.; Ogura, M.; Okushi, H.; Nothaft, M.; Neumann, P.; Gali, A.; Jelezko, F.; et al. Electrically Driven Single-Photon Source at Room Temperature in Diamond. *Nat. Photonics* **2012**, *6*, 299−303.
(8) Gao, T.; von Helversen, M.; Antón-Solanas, C.; Schneider, C.; Heindel, T. Atomically-Thin Single-Photon Sources for Quantum Communication. *Npj 2D Mater. Appl.* **2023**, *7*, No. 4.
(9) Gupta, S.; Wu, W.; Huang, S.; Yakobson, B. I. Single-Photon Emission from Two-Dimensional Materials, to a Brighter Future. *J. Phys. Chem. Lett.* **2023**, *14*, 3274−3284.
(10) Zhang, L.; Yu, Y.-J.; Chen, L.-G.; Luo, Y.; Yang, B.; Kong, F.-F.; Chen, G.; Zhang, Y.; Zhang, Q.; Luo, Y.; et al. Electrically Driven Single-Photon Emission from an Isolated Single Molecule. *Nat. Commun.* **2017**, *8*, No. 580.
(11) Toninelli, C.; Gerhardt, I.; Clark, A. S.; Reserbat-Plantey, A.; Götzinger, S.; Ristanović, Z.; Colautti, M.; Lombardi, P.; Major, K. D.; Deperasińska, I.; et al. Single Organic Molecules for Photonic Quantum Technologies. *Nat. Mater.* **2021**, *20*, 1615−1628.
(12) Thomas, S. E.; Wagner, L.; Joos, R.; Sittig, R.; Nawrath, C.; Burdekin, P.; de Buy Wenniger, I. M.; Rasiah, M. J.; Huber-Loyola, T.; Sagona-Stophel, S.; et al. Deterministic Storage and Retrieval of Telecom Light from a Quantum Dot Single-Photon Source Interfaced with an Atomic Quantum Memory. *Sci. Adv.* **2023**, *10*, No. eadi7346.
(13) Michler, P.; Imamoğlu, A.; Mason, M. D.; Carson, P. J.; Strouse, G. F.; Buratto, S. K. Quantum Correlation among Photons from a Single Quantum Dot at Room Temperature. *Nature* **2000**, *406*, 968−970.
(14) Chen, Y.; Sharp, D.; Saxena, A.; Nguyen, H.; Cossairt, B. M.; Majumdar, A. Integrated Quantum Nanophotonics with Solution-Processed Materials. *Adv. Quantum Technol.* **2022**, *5*, No. 2100078.
(15) Kagan, C. R.; Bassett, L. C.; Murray, C. B.; Thompson, S. M. Colloidal Quantum Dots as Platforms for Quantum Information Science. *Chem. Rev.* **2021**, *121*, 3186−3233.
(16) Uppu, R.; Midolo, L.; Zhou, X.; Carolan, J.; Lodahl, P. Quantum-Dot-Based Deterministic Photon−Emitter Interfaces for Scalable Photonic Quantum Technology. *Nat. Nanotechnol.* **2021**, *16*, 1308−1317.
(17) Nguyen, H. A.; Sharp, D.; Fröch, J. E.; Cai, Y.-Y.; Wu, S.; Monahan, M.; Munley, C.; Manna, A.; Majumdar, A.; Kagan, C. R.; Cossairt, B. M. Deterministic Quantum Light Arrays from Giant Silica-Shelled Quantum Dots. *ACS Appl. Mater. Interfaces* **2023**, *15*, 4294−4302.
(18) Utzat, H.; Sun, W.; Kaplan, A. E. K.; Krieg, F.; Ginterseder, M.; Spokoyny, B.; Klein, N. D.; Shulenberger, K. E.; Perkinson, C. F.; Kovalenko, M. V.; Bawendi, M. G. Coherent Single-Photon Emission from Colloidal Lead Halide Perovskite Quantum Dots. *Science* **2019**, *363*, 1068−1072.
(19) Becker, M. A.; Scarpelli, L.; Nedelcu, G.; Rainò, G.; Masia, F.; Borri, P.; Stöferle, T.; Kovalenko, M. V.; Langbein, W.; Mahrt, R. F. Long Exciton Dephasing Time and Coherent Phonon Coupling in CsPbBr2Cl Perovskite Nanocrystals. *Nano Lett.* **2018**, *18*, 7546−7551.
(20) Nguyen, H. A.; Dixon, G.; Dou, F. Y.; Gallagher, S.; Gibbs, S.; Ladd, D. M.; Marino, E.; Ondry, J. C.; Shanahan, J. P.; Vasileiadou, E. S.; et al. Design Rules for Obtaining Narrow Luminescence from Semiconductors Made in Solution. *Chem. Rev.* **2023**, *123*, 7890−7952.
(21) Song, Y.; Liu, R.; Wang, Z.; Xu, H.; Ma, Y.; Fan, F.; Voznyy, O.; Du, J. Enhanced Emission Directivity from Asymmetrically Strained Colloidal Quantum Dots. *Sci. Adv.* **2022**, *8*, No. eabl8219.
(22) Geiregat, P.; Van Thourhout, D.; Hens, Z. A Bright Future for Colloidal Quantum Dot Lasers. *NPG Asia Mater.* **2019**, *11*, No. 41.
(23) Saxena, A.; Chen, Y.; Ryou, A.; Sevilla, C. G.; Xu, P.; Majumdar, A. Improving Indistinguishability of Single Photons from Colloidal Quantum Dots Using Nanocavities. *ACS Photonics* **2019**, *6*, 3166−3173.
(24) Zhu, C.; Marczak, M.; Feld, L.; Boehme, S. C.; Bernasconi, C.; Moskalenko, A.; Cherniukh, I.; Dirin, D.; Bodnarchuk, M. I.; Kovalenko, M. V.; Rainò, G. Room-Temperature, Highly Pure Single-Photon Sources from All-Inorganic Lead Halide Perovskite Quantum Dots. *Nano Lett.* **2022**, *22*, 3751−3760.
(25) Hsu, B.-W.; Chuang, Y.-T.; Cheng, C.-Y.; Chen, C.-Y.; Chen, Y.-J.; Brumberg, A.; Yang, L.; Huang, Y.-S.; Schaller, R. D.; Chen, L.-J.; et al. Very Robust Spray-Synthesized CsPbI3 Quantum Emitters with Ultrahigh Room-Temperature Cavity-Free Brightness and Self-Healing Ability. *ACS Nano* **2021**, *15*, 11358−11368.
(26) Park, Y.-S.; Guo, S.; Makarov, N. S.; Klimov, V. I. Room Temperature Single-Photon Emission from Individual Perovskite Quantum Dots. *ACS Nano* **2015**, *9*, 10386−10393.
(27) O'Brien, J. L.; Furusawa, A.; Vučković, J. Photonic Quantum Technologies. *Nat. Photonics* **2009**, *3*, 687−695.
(28) Gupta, S.; Waks, E. Spontaneous Emission Enhancement and Saturable Absorption of Colloidal Quantum Dots Coupled to Photonic Crystal Cavity. *Opt. Express* **2013**, *21*, 29612−29619.
(29) Jun, S.; Kim, J.; Choi, M.; Kim, B. S.; Park, J.; Kim, D.; Shin, B.; Cho, Y.-H. Ultrafast and Bright Quantum Emitters from the Cavity-Coupled Single Perovskite Nanocrystals. *ACS Nano* **2024**, *18*, 1396−1403.
(30) Chen, Y.; Ryou, A.; Friedfeld, M. R.; Fryett, T.; Whitehead, J.; Cossairt, B. M.; Majumdar, A. Deterministic Positioning of Colloidal Quantum Dots on Silicon Nitride Nanobeam Cavities. *Nano Lett.* **2018**, *18*, 6404−6410.
(31) Schell, A. W.; Kewes, G.; Schröder, T.; Wolters, J.; Aichele, T.; Benson, O. A Scanning Probe-Based Pick-and-Place Procedure for Assembly of Integrated Quantum Optical Hybrid Devices. *Rev. Sci. Instrum.* **2011**, *82*, No. 073709.
(32) Kim, J.-H.; Aghaeimeibodi, S.; Richardson, C. J. K.; Leavitt, R. P.; Englund, D.; Waks, E. Hybrid Integration of Solid-State Quantum Emitters on a Silicon Photonic Chip. *Nano Lett.* **2017**, *17*, 7394−7400.
(33) Barth, M.; Schietinger, S.; Fischer, S.; Becker, J.; Nüsse, N.; Aichele, T.; Löchel, B.; Sönnichsen, C.; Benson, O. Nanoassembled Plasmonic-Photonic Hybrid Cavity for Tailored Light-Matter Coupling. *Nano Lett.* **2010**, *10*, 891−895.
(34) Choi, M.; Lee, M.; Park, S.-Y. L.; Kim, B. S.; Jun, S.; Park, S. I.; Song, J. D.; Ko, Y.-H.; Cho, Y.-H. Single Quantum Dot Selection and Tailor-Made Photonic Device Integration Using a Nanoscale-Focus Pinspot. *Adv. Mater.* **2023**, *35*, No. 2210667.
(35) Xie, W.; Gomes, R.; Aubert, T.; Bisschop, S.; Zhu, Y.; Hens, Z.; Brainis, E.; Van Thourhout, D. Nanoscale and Single-Dot Patterning of Colloidal Quantum Dots. *Nano Lett.* **2015**, *15*, 7481−7487.
(36) Reiss, P.; Protière, M.; Li, L. Core/Shell Semiconductor Nanocrystals. *Small* **2009**, *5*, 154−168.
(37) Nann, T.; Mulvaney, P. Single Quantum Dots in Spherical Silica Particles. *Angew. Chem., Int. Ed.* **2004**, *43*, 5393−5396.
(38) Sampat, S.; Karan, N. S.; Guo, T.; Htoon, H.; Hollingsworth, J. A.; Malko, A. V. Multistate Blinking and Scaling of Recombination Rates in Individual Silica-Coated CdSe/CdS Nanocrystals. *ACS Photonics* **2015**, *2*, 1505−1512.

https://doi.org/10.1021/acsnano.4c06961
ACS Nano 2024, 18, 20726−20739

(39) Chen, Y.; Vela, J.; Htoon, H.; Casson, J. L.; Werder, D. J.; Bussian, D. A.; Klimov, V. I.; Hollingsworth, J. A. Giant" Multishell CdSe Nanocrystal Quantum Dots with Suppressed Blinking. *J. Am. Chem. Soc.* **2008**, *130*, 5026−5027.
(40) Singh, A.; Majumder, S.; Orfield, N. J. T.; Sarpkaya, I.; Nordlund, D.; Bustillo, K. C.; Ciston, J.; Nisoli, V.; Ivanov, S. A.; Bowes, E. G.; et al. From Inside Out: How the Buried Interface, Shell Defects, and Surface Chemistry Conspire to Determine Optical Performance in Nonblinking Giant Quantum Dots. *Small Sci.* **2023**, *3*, No. 2300092.
(41) Bladt, E.; van Dijk-Moes, R. J. A.; Peters, J.; Montanarella, F.; de Mello Donega, C.; Vanmaekelbergh, D.; Bals, S. Atomic Structure of Wurtzite CdSe (Core)/CdS (Giant Shell) Nanobullets Related to Epitaxy and Growth. *J. Am. Chem. Soc.* **2016**, *138*, 14288−14293.
(42) Nasilowski, M.; Spinicelli, P.; Patriarche, G.; Dubertret, B. Gradient CdSe/CdS Quantum Dots with Room Temperature Biexciton Unity Quantum Yield. *Nano Lett.* **2015**, *15*, 3953−3958.
(43) Galland, C.; Ghosh, Y.; Steinbrück, A.; Hollingsworth, J. A.; Htoon, H.; Klimov, V. I. Lifetime Blinking in Nonblinking Nanocrystal Quantum Dots. *Nat. Commun.* **2012**, *3*, No. 908.
(44) García-Santamaría, F.; Chen, Y.; Vela, J.; Schaller, R. D.; Hollingsworth, J. A.; Klimov, V. I. Suppressed Auger Recombination in "Giant" Nanocrystals Boosts Optical Gain Performance. *Nano Lett.* **2009**, *9*, 3482−3488.
(45) Pal, B. N.; Ghosh, Y.; Brovelli, S.; Laocharoensuk, R.; Klimov, V. I.; Hollingsworth, J. A.; Htoon, H. Giant' CdSe/CdS Core/Shell Nanocrystal Quantum Dots As Efficient Electroluminescent Materials: Strong Influence of Shell Thickness on Light-Emitting Diode Performance. *Nano Lett.* **2012**, *12*, 331−336.
(46) Diroll, B. T.; Hua, M.; Guzelturk, B.; Pálmai, M.; Tomczak, K. Long-Lived and Bright Biexcitons in Quantum Dots with Parabolic Band Potentials. *Nano Lett.* **2023**, *23*, 11975−11981.
(47) Matsuzaki, K.; Vassant, S.; Liu, H.-W.; Dutschke, A.; Hoffmann, B.; Chen, X.; Christiansen, S.; Buck, M. R.; Hollingsworth, J. A.; Götzinger, S.; Sandoghdar, V. Strong Plasmonic Enhancement of Biexciton Emission: Controlled Coupling of a Single Quantum Dot to a Gold Nanocone Antenna. *Sci. Rep.* **2017**, *7*, No. 42307.
(48) Park, Y.-S.; Malko, A. V.; Vela, J.; Chen, Y.; Ghosh, Y.; García-Santamaría, F.; Hollingsworth, J. A.; Klimov, V. I.; Htoon, H. Near-Unity Quantum Yields of Biexciton Emission from CdSe/CdS Nanocrystals Measured Using Single-Particle Spectroscopy. *Phys. Rev. Lett.* **2011**, *106*, No. 187401.
(49) Hanifi, D. A.; Bronstein, N. D.; Koscher, B. A.; Nett, Z.; Swabeck, J. K.; Takano, K.; Schwartzberg, A. M.; Maserati, L.; Vandewal, K.; van de Burgt, Y.; et al. Redefining Near-Unity Luminescence in Quantum Dots with Photothermal Threshold Quantum Yield. *Science* **2019**, *363*, 1199−1202.
(50) Hollingsworth, J. A. Heterostructuring Nanocrystal Quantum Dots Toward Intentional Suppression of Blinking and Auger Recombination. *Chem. Mater.* **2013**, *25*, 1318−1331.
(51) Ghosh, Y.; Mangum, B. D.; Casson, J. L.; Williams, D. J.; Htoon, H.; Hollingsworth, J. A. New Insights into the Complexities of Shell Growth and the Strong Influence of Particle Volume in Nonblinking "Giant" Core/Shell Nanocrystal Quantum Dots. *J. Am. Chem. Soc.* **2012**, *134*, 9634−9643.
(52) Tan, R.; Yuan, Y.; Nagaoka, Y.; Eggert, D.; Wang, X.; Thota, S.; Guo, P.; Yang, H.; Zhao, J.; Chen, O. Monodisperse Hexagonal Pyramidal and Bipyramidal Wurtzite CdSe-CdS Core−Shell Nanocrystals. *Chem. Mater.* **2017**, *29*, 4097−4108.
(53) Chen, O.; Zhao, J.; Chauhan, V. P.; Cui, J.; Wong, C.; Harris, D. K.; Wei, H.; Han, H.-S.; Fukumura, D.; Jain, R. K.; Bawendi, M. G. Compact High-Quality CdSe−CdS Core−Shell Nanocrystals with Narrow Emission Linewidths and Suppressed Blinking. *Nat. Mater.* **2013**, *12*, 445−451.
(54) Cirillo, M.; Aubert, T.; Gomes, R.; Van Deun, R.; Emplit, P.; Biermann, A.; Lange, H.; Thomsen, C.; Brainis, E.; Hens, Z. Flash" Synthesis of CdSe/CdS Core−Shell Quantum Dots. *Chem. Mater.* **2014**, *26*, 1154−1160.
(55) Christodoulou, S.; Vaccaro, G.; Pinchetti, V.; De Donato, F.; Grim, J. Q.; Casu, A.; Genovese, A.; Vicidomini, G.; Diaspro, A.; Brovelli, S.; et al. Synthesis of Highly Luminescent Wurtzite CdSe/CdS Giant-Shell Nanocrystals Using a Fast Continuous Injection Route. *J. Mater. Chem. C* **2014**, *2*, 3439−3447.
(56) Wang, X.; Liu, M.; Zhou, Z.; Guo, L. Toward Facet Engineering of CdS Nanocrystals and Their Shape-Dependent Photocatalytic Activities. *J. Phys. Chem. C* **2015**, *119*, 20555−20560.
(57) Lei, H.; Li, T.; Li, J.; Zhu, J.; Zhang, H.; Qin, H.; Kong, X.; Wang, L.; Peng, X. Reversible Facet Reconstruction of CdSe/CdS Core/Shell Nanocrystals by Facet−Ligand Pairing. *J. Am. Chem. Soc.* **2023**, *145*, 6798−6810.
(58) Ji, B.; Panfil, Y. E.; Waiskopf, N.; Remennik, S.; Popov, I.; Banin, U. Strain-Controlled Shell Morphology on Quantum Rods. *Nat. Commun.* **2019**, *10*, No. 2.
(59) Kong, X.; Yu, F.; Zhang, H.; Lv, F.; Wang, Y.; Yin, L.; Huang, J.; Feng, Q. Synthesis and Study of Morphology Regulation, Formation Mechanism and Photocatalytic Performance of CdS. *Appl. Surf. Sci.* **2022**, *576*, No. 151817.
(60) Momma, K.; Izumi, F. VESTA3 for Three-Dimensional Visualization of Crystal, Volumetric and Morphology Data. *J. Appl. Crystallogr.* **2011**, *44*, 1272−1276.
(61) Rempel, J. Y.; Trout, B. L.; Bawendi, M. G.; Jensen, K. F. Properties of the CdSe(0001), (000$\bar{1}$), and (11$\bar{2}$0) Single Crystal Surfaces: Relaxation, Reconstruction, and Adatom and Admolecule Adsorption. *J. Phys. Chem. B* **2005**, *109*, 19320−19328.
(62) Hughes, S. M.; Alivisatos, A. P. Anisotropic Formation and Distribution of Stacking Faults in II−VI Semiconductor Nanorods. *Nano Lett.* **2013**, *13*, 106−110.
(63) Alpay, D.; Peng, L.; Marks, L. D. Are Nanoparticle Corners Round? *J. Phys. Chem. C* **2015**, *119*, 21018−21023.
(64) Coropceanu, I.; Bawendi, M. G. Core/Shell Quantum Dot Based Luminescent Solar Concentrators with Reduced Reabsorption and Enhanced Efficiency. *Nano Lett.* **2014**, *14*, 4097−4101.
(65) Zhou, X.; Pu, C. Proton Shuttle-Assisted Surface Reconstruction toward Nonpolar Facets-Terminated Zinc-Blende CdSe/CdS Core/Shell Quantum Dots. *J. Am. Chem. Soc.* **2023**, *145*, 26287−26295.
(66) Zhou, J.; Pu, C.; Jiao, T.; Hou, X.; Peng, X. A Two-Step Synthetic Strategy toward Monodisperse Colloidal CdSe and CdSe/CdS Core/Shell Nanocrystals. *J. Am. Chem. Soc.* **2016**, *138*, 6475−6483.
(67) Xu, J. X.; Yuan, Y.; Liu, M.; Zou, S.; Chen, O.; Zhang, D. Quantification of the Photon Absorption, Scattering, and On-Resonance Emission Properties of CdSe/CdS Core/Shell Quantum Dots: Effect of Shell Geometry and Volumes. *Anal. Chem.* **2020**, *92*, 5346−5353.
(68) Piri, N.; Shams-Nateri, A.; Mokhtari, J. The Relationship between Refractive Index and Optical Properties of Absorbing Nanoparticle. *Color Res. Appl.* **2016**, *41*, 477−483.
(69) Cho, J.; Jung, Y. K.; Lee, J.-K.; Jung, H.-S. Highly Efficient Blue-Emitting CdSe-Derived Core/Shell Gradient Alloy Quantum Dots with Improved Photoluminescent Quantum Yield and Enhanced Photostability. *Langmuir* **2017**, *33*, 3711−3719.
(70) Bae, W. K.; Nam, M. K.; Char, K.; Lee, S. Gram-Scale One-Pot Synthesis of Highly Luminescent Blue Emitting Cd1−xZnxS/ZnS Nanocrystals. *Chem. Mater.* **2008**, *20*, 5307−5313.
(71) Singh, R.; Akhil, S.; Dutt, V. G. V.; Mishra, N. Shell Thickness Dependent Photostability Studies of Green-Emitting "Giant" Quantum Dots. *Nanoscale Adv.* **2021**, *3*, 6984−6991.
(72) Würth, C.; Resch-Genger, U. Determination of Photoluminescence Quantum Yields of Scattering Media with an Integrating Sphere: Direct and Indirect Illumination. *Appl. Spectrosc.* **2015**, *69*, 749−759.
(73) García-Santamaría, F.; Brovelli, S.; Viswanatha, R.; Hollingsworth, J. A.; Htoon, H.; Crooker, S. A.; Klimov, V. I. Breakdown of Volume Scaling in Auger Recombination in CdSe/CdS Heteronanocrystals: The Role of the Core−Shell Interface. *Nano Lett.* **2011**, *11*, 687−693.

https://doi.org/10.1021/acsnano.4c06961
ACS Nano 2024, 18, 20726−20739

(74) Qin, H.; Meng, R.; Wang, N.; Peng, X. Photoluminescence Intermittency and Photo-Bleaching of Single Colloidal Quantum Dot. *Adv. Mater.* **2017**, *29*, No. 1606923.
(75) Fisher, B.; Caruge, J. M.; Zehnder, D.; Bawendi, M. Room-Temperature Ordered Photon Emission from Multiexciton States in Single CdSe Core-Shell Nanocrystals. *Phys. Rev. Lett.* **2005**, *94*, No. 087403.
(76) Cohen, T. A.; Sharp, D.; Kluherz, K. T.; Chen, Y.; Munley, C.; Anderson, R. T.; Swanson, C. J.; De Yoreo, J. J.; Luscombe, C. K.; Majumdar, A.; et al. Direct Patterning of Perovskite Nanocrystals on Nanophotonic Cavities with Electrohydrodynamic Inkjet Printing. *Nano Lett.* **2022**, *22*, 5681−5688.
(77) Guymon, G. G.; Sharp, D.; Cohen, T. A.; Gibbs, S. L.; Manna, A.; Tzanetopoulos, E.; Gamelin, D. R.; Majumdar, A.; MacKenzie, J. D. Electrohydrodynamic Printing-Based Heterointegration of Quantum Dots on Suspended Nanophotonic Cavities. *Adv. Mater. Technol.* **2024**, *9*, No. 2301921.
(78) Barad, H.-N.; Kwon, H.; Alarcón-Correa, M.; Fischer, P. Large Area Patterning of Nanoparticles and Nanostructures: Current Status and Future Prospects. *ACS Nano* **2021**, *15*, 5861−5875.
(79) Shulevitz, H. J.; Huang, T.-Y.; Xu, J.; Neuhaus, S. J.; Patel, R. N.; Choi, Y. C.; Bassett, L. C.; Kagan, C. R. Template-Assisted Self-Assembly of Fluorescent Nanodiamonds for Scalable Quantum Technologies. *ACS Nano* **2022**, *16*, 1847−1856.
(80) Greybush, N. J.; Pacheco-Peña, V.; Engheta, N.; Murray, C. B.; Kagan, C. R. Plasmonic Optical and Chiroptical Response of Self-Assembled Au Nanorod Equilateral Trimers. *ACS Nano* **2019**, *13*, 1617−1624.
(81) Jasieniak, J.; Smith, L.; van Embden, J.; Mulvaney, P.; Califano, M. Re-Examination of the Size-Dependent Absorption Properties of CdSe Quantum Dots. *J. Phys. Chem. C* **2009**, *113*, 19468−19474.
(82) Li, C.; Tardajos, A. P.; Wang, D.; Choukroun, D.; Van Daele, K.; Breugelmans, T.; Bals, S. A Simple Method to Clean Ligand Contamination on TEM Grids. *Ultramicroscopy* **2021**, *221*, No. 113195.
(83) MessaoudiI, C.; Boudier, T.; Sorzano, C. O. S.; Marco, S. TomoJ: Tomography Software for Three-Dimensional Reconstruction in Transmission Electron Microscopy. *BMC Bioinf.* **2007**, *8*, No. 288.
(84) Schmid, B.; Schindelin, J.; Cardona, A.; Longair, M.; Heisenberg, M. A High-Level 3D Visualization API for Java and ImageJ. *BMC Bioinf.* **2010**, *11*, No. 274.
(85) De Backer, A.; van den Bos, K. H. W.; Van den Broek, W.; Sijbers, J.; Van Aert, S. StatSTEM: An Efficient Approach for Accurate and Precise Model-Based Quantification of Atomic Resolution Electron Microscopy Images. *Ultramicroscopy* **2016**, *171*, 104−116.
(86) Madsen, J.; Susi, T. The ab TEM Code: Transmission Electron Microscopy from First Principles *Open Res. Eur.* 2021; Vol. *124* DOI: 10.12688/openreseurope.13015.2.
(87) Yaman, M. Y.; Guye, K. N.; Ziatdinov, M.; Shen, H.; Baker, D.; Kalinin, S. V.; Ginger, D. S. Alignment of Au Nanorods along de Novo Designed Protein Nanofibers Studied with Automated Image Analysis. *Soft Matter* **2021**, *17*, 6109−6115.
(88) Gallagher, S.; Kline, J.; Jahanbakhshi, F.; Sadighian, J. C.; Lyons, I.; Shen, G.; Rappe, A. M.; Ginger, D. S. Ligand Equilibrium Influences Photoluminescence Blinking in CsPbBr3: A Change Point Analysis of Widefield Imaging Data. *ACS Nano* **2024**, *18*, 19208−19219.

https://doi.org/10.1021/acsnano.4c06961
ACS Nano 2024, 18, 20726−20739